High-frequency vibrational dynamics in glasses

2001 J. Phys.: Condens. Matter 13 9141

(http://iopscience.iop.org/0953-8984/13/41/307)

INSTITUTE OF PHYSICS PUBLISHING JOURNAL OF PHYSICS: CONDENSED MATTER

J. Phys.: Condens. Matter **13** (2001) 9141–9164 PII: S0953-8984(01)25896-2

High-frequency vibrational dynamics in glasses

Giancarlo Ruocco[1] **and Francesco Sette**[2]

[1] Dipartimento di Fisica and INFM, Università di Roma 'La Sapienza', I-00185, Roma, Italy
[2] European Synchrotron Radiation Facility, BP 220, F-38043, Grenoble Cédex, France

Received 19 June 2001
Published 28 September 2001
Online at stacks.iop.org/JPhysCM/13/9141

Abstract

In this paper we present a review of the recent inelastic x-ray scattering (IXS) studies on the high-frequency collective dynamics in topologically disordered systems. At mesoscopic exchanged momenta ($Q \approx 1$–10 nm^{-1}), these IXS studies allowed experimental demonstration of the existence in glasses of propagating acoustic phonon-like excitations whose characteristics are *qualitatively* independent from the specific system investigated. These universal features are as follows: (i) on the small-Q side of the momentum region examined, the existence of a linear dispersion for the excitation frequency of the longitudinal excitations; this dispersion starts to bend downward with increasing Q-value; (ii) a quadratic Q-dependence of the excitation width, $\Gamma(Q)$, in the Q-region where $\Omega(Q)$ is linear; (iii) temperature independence of this excitation; and (iv) the appearance—with increasing Q-value—of the signature of the collective transverse dynamics. In this paper, using the case of vitreous silica as a representative example, we present the IXS evidence for these universal features and we compare them with the outcome of computer simulations. Finally, we will show that all the observed characteristics of the high-frequency vibrations can be retrieved within the 'harmonic' approximation of the glass dynamics.

1. Introduction

The discovery that disordered materials, such as glasses and liquids, support the propagation of sound waves in the *terahertz* frequency region has renewed interest in a long-standing issue: the nature of collective excitations in disordered solids. In the last few years, progress in the understanding of this subject was achieved with the aid of new experimental facilities, improved numerical techniques, and, more recently, new theoretical tools [1, 2].

From the experimental point of view, the collective excitations are often studied through the determination of the dynamic structure factor $S(Q, \omega)$, i.e. the time Fourier transform of the collective intermediate-scattering function $F(Q, t)$ which, in turn, is the space Fourier transform of the density self-correlation function. $S(Q, \omega)$ has been widely studied in the past by the Brillouin light scattering (BLS) and inelastic neutron scattering (INS) techniques.

In the BLS technique, the accessible exchanged momenta (Q) are limited to the range $Q < 10^{-2}$ nm^{-1} because of the momentum carried by visible light photons. In INS, due to the kinematic limitation associated with the neutron mass, the small-Q range is not accessible and the allowed Q–ω region does not cover the dispersion relation of the collective excitations, except for a few favourable systems with not-too-high sound velocity. Previous techniques left an unexplored gap in the Q-space, corresponding to exchanged momentum approaching the inverse of the inter-particle separation a (the mesoscopic region, $Q = 1$–10 nm^{-1}). This Q-region is important, because here the collective dynamics undergoes a transition from a hydrodynamic behaviour to a microscopic single-particle one. Investigation of $S(Q, \omega)$ in this mesoscopic region has become possible recently thanks to the development of the IXS technique [3]; many systems, ranging from glasses [3–12] to liquids [13,14], have been studied with this technique. In addition to specific *quantitative* differences among different systems, all the glasses investigated show some *qualitative* common features that can be summarized as follows:

(i) Propagating acoustic-like excitations exist up to a maximum Q-value Q_m ($Q_m a \approx 1$–3 depending on the system fragility). Similarly to well defined peaks, they have an excitation frequency $\Omega(Q)$.
(ii) $\Omega(Q)$ versus Q shows an almost linear dispersion relation, and its slope, in the $Q \to 0$ limit, extrapolates to the macroscopic sound velocity.
(iii) The width of the Brillouin peaks, $\Gamma(Q)$, follows a power law, $\Gamma(Q) = DQ^{\alpha}$, with $\alpha = 2$ within the currently available statistical accuracy.
(iv) The value of D does not depend significantly on temperature, indicating that this broadening (i.e. the sound attenuation) in the high-frequency region does not have a dynamic origin, but is instead due to the disorder [15].
(v) Finally, at large Q-values, a second peak appears in $S(Q, \omega)$ at frequencies smaller than that of the longitudinal acoustic excitations. This peak can be ascribed to the transverse acoustic dynamics, whose signature is observed in the dynamic structure factor as a consequence of the absence of pure polarization of the vibrations in a topologically disordered system.

These general features of $S(Q, \omega)$ have been confirmed by numerical calculations, both via standard molecular dynamics (MD) simulations of glasses and via normal-mode analysis (NMA) within the *harmonic approximation* of the glasses themselves [16–19]. Larger and larger systems have been investigated in the last few years thanks to the improved computing facilities and to the application of new numerical schemes, such as the method of moments [20], to evaluate $S(Q, \omega)$. The numerical simulations also allowed clarification of an important issue concerning the origin of the sound attenuation (i.e. the excitation broadening) in glasses. In particular, by comparing numerical simulations of topologically disordered systems with those of substitutionally disordered ones, it has been shown that—in the 'true' topologically disordered systems—the excitation broadening follows a Q^2-law, while $\Gamma(Q)$ shows a Q^4-dependence in the case of substitutional (or lattice) disorder [21–24].

More recently Götze *et al* extended the mode-coupling theory (MCT) calculation scheme to the case of the non-ergodic, glassy phase. This theory, as shown numerically for a hard-sphere model, accounts for all the features of the dynamic structure factor listed above. A further prediction of the theory, namely the presence of a positive dispersion of the sound velocity, i.e. a small upwards bend of the dispersion relation, has not yet been experimentally detected. In subsequent MD investigations this positive dispersion of the sound velocity has been observed. In fact, it has been tentatively ascribed to a relaxation process taking place in harmonic disordered systems [25]. This interpretation, at first sight, could seem to present

a contradiction, because the 'relaxation processes' concept is usually related to phenomena like 'viscous flow' and 'anharmonicity', and it is difficult to understand the meaning of a relaxation process in a harmonic system. This has allowed extension of the concept of 'relaxation process'. In fact, on general grounds, a relaxation process can be pictured as the macroscopic manifestation of microscopic phenomena allowing the energy stored in a given 'mode' to relax towards other degrees of freedom. $S(Q, \omega)$, as can be seen for example through the fluctuation-dissipation relation, reflects the time evolution of the energy initially stored ($t = t_0$) in a plane wave (PW) of wavelength $2\pi/Q$. As the PW is certainly not an eigenstate of the disordered system, at $t > t_0$ there will be a transfer of amplitude from this PW towards other PWs of different Q-values. This process is controlled by the projection of the PW considered into the true normal modes of the topologically disordered glassy structure, and the flow takes place on a timescale τ which is also determined by these projections. This mechanism gives rise to the observed relaxation process phenomenology.

In this article we illustrate the state-of-the-art inelastic x-ray scattering (IXS) studies on the collective excitations in glasses by using the specific case of vitreous silica, v-SiO_2, as an example. Vitreous silica, besides being the best known example of *glass*, is particularly relevant in the present context. Indeed, while on one hand the above-mentioned universal characteristics of the high-frequency dynamics are nowadays recognized by the scientific community to be valid in most of systems investigated, v-SiO_2 represents an exception, and at least two different interpretations of the IXS data exist[3]. It is our aim to present a critical review of the existing data and their interpretations. To this end, we will also make use of the results of a molecular dynamics simulation study of v-SiO_2. In the next section we will show how—and to what degree of approximation—the IXS experiment determines the dynamic structure factors. We also discuss the experimental set-up. In the following section we give the theoretical background, aiming to put the interpretation of the dynamic structure factor of disordered systems in terms of few statistical mechanics principles on a sound basis. Then we will present a few details of the MD investigations and the results obtained in the specific case of vitreous silica.

2. The IXS experiment

2.1. IXS: what does the technique measure?

An IXS experiment is based on a scattering process where a beam of photons, prepared with energy $\hbar\omega_i$, momentum $\hbar\boldsymbol{k}_i$, and polarization $\boldsymbol{\epsilon}_i$, impinge on a sample, and one detects the photons scattered with a specific energy $\hbar\omega_f$, momentum $\hbar\boldsymbol{k}_f$, and polarization $\boldsymbol{\epsilon}_f$. The scattered photons carry information on the spectrum of the excitations of energy $\hbar\omega = \hbar\omega_i - \hbar\omega_f$ and momentum $\hbar\boldsymbol{Q} = \hbar\boldsymbol{k}_i - \hbar\boldsymbol{k}_f$ which are created (or destroyed) in the target during the interaction. In the limit of weak interaction between the photons and the sample, the scattering process can be described in the framework of the linear response theory. Here, the differential scattering cross-section per unit frequency ω and unit solid angle, Ω, $\partial^2\sigma/\partial\omega\,\partial\Omega$, is determined by a perturbation treatment of the photon–electron interaction Hamiltonian. In the case of photons in the $\approx$10 keV range, in the absence of resonant conditions and considering energies $\hbar\omega$ in the range of the typical acoustic photon energies (less than $\approx$100 meV), the

[3] The interpretation of the vitreous silica IXS data along the same lines as for all the other glasses can be found in references [6, 9, 10, 12]. An alternative interpretation, where the broadening of the excitations is supposed to follow a $\Gamma(Q) \propto Q^4$ law, is reported in references [5, 11]. It worth noting that a completely different interpretation of the IXS spectra in glasses is proposed in reference [26].

radiation–electron interaction Hamiltonian reduces to the Thomson term:

$$H_{int} = \frac{1}{2} r_0 \sum_j \boldsymbol{A}^2(\boldsymbol{r}_j, t) \tag{1}$$

where $r_0 = e^2/m_e c^2$ is the classical electron radius, e is the electron charge, m_e is the electron mass, $\boldsymbol{A}(\boldsymbol{r}, t)$ is the electromagnetic field potential vector, and $\boldsymbol{r}_j$ is the position of the jth electron in the sample. We have neglected

(i) the so-called 'magnetic' terms, that arise from the coupling of the electromagnetic field with the electron spin and whose order of magnitude is $\approx \hbar\omega_i/m_e c^2$ smaller than the Thomson term;
(ii) the $\boldsymbol{\nabla} \cdot \boldsymbol{A}(\boldsymbol{r}, t)$ term, which is relevant in resonant conditions and vanishing in the $\omega \ll \omega_i$ limit of interest here; and
(iii) the direct photon–nuclei interaction term, whose order of magnitude is m_e/m_n smaller than the photon–electron interaction term of equation (1). Here m_n is the nuclear mass.

On applying the first-order perturbation theory—or the Fermi golden rule—and the adiabatic approximation (i.e. the factorization of the electronic and nuclear eigenstates), one gets

$$\frac{\partial^2\sigma}{\partial\omega\,\partial\Omega} = r_0^2(\boldsymbol{\epsilon}_i \cdot \boldsymbol{\epsilon}_f)^2 \frac{k_i}{k_f} \sum_{I_n, F_n} P_{I_n} |\langle F_n| \sum_j f_j(\boldsymbol{Q}) \mathrm{e}^{\mathrm{i}\boldsymbol{Q}\cdot\boldsymbol{R}_j} |I_n\rangle|^2 \delta(\omega - \omega_f - \omega_i). \tag{2}$$

Here $|I_n\rangle$ ($|F_n\rangle$) are the initial (final) nuclear states; P_{I_n} represents the thermal population of the initial states and $f_j(\boldsymbol{Q})$ is the form factor of the jth particle whose centre-of-mass position is $\boldsymbol{R}_j$. The form factor is the space Fourier transform of the electron-density distribution. In the case of a monatomic system, $f_j(\boldsymbol{Q}) = f(Q)$ independently on the jth atom, and equation (2) can be related to the dynamic structure factor, $S(Q, \omega)$, for which the expression is

$$S(Q, \omega) = \frac{1}{N} \sum_{I_n, F_n} P_{I_n} |\langle F_n| \sum_j \mathrm{e}^{\mathrm{i}\boldsymbol{Q}\cdot\boldsymbol{R}_j} |I_n\rangle|^2 \delta(\omega - \omega_f - \omega_i). \tag{3}$$

In fact the scattering cross-section can be written as

$$\frac{\partial^2\sigma}{\partial\omega\,\partial\Omega} = N r_0^2(\boldsymbol{\epsilon}_i \cdot \boldsymbol{\epsilon}_f)^2 \frac{k_i}{k_f} |f(Q)|^2 S(Q, \omega) \tag{4}$$

and thus—in this simple case of monatomic systems—the inelastic x-ray scattering cross-section is directly proportional to $S(Q, \omega)$. In cases—like that of vitreous silica—where more than one atomic species is present in the sample, one defines a *partial* dynamic structure factor, $S_{\alpha\beta}(Q, \omega)$, as follows (here α and β label the atomic species):

$$S_{\alpha\beta}(Q, \omega) = \frac{1}{N} \sum_{I_n, F_n} P_{I_n} \sum_{ij} \langle F_n| \mathrm{e}^{\mathrm{i}\boldsymbol{Q}\cdot\boldsymbol{R}_i^{\alpha}} |I_n\rangle \langle I_n| \mathrm{e}^{-\mathrm{i}\boldsymbol{Q}\cdot\boldsymbol{R}_j^{\beta}} |F_n\rangle \delta(\omega - \omega_f - \omega_i) \tag{5}$$

and the scattering cross-section is given by

$$\frac{\partial^2\sigma}{\partial\omega\,\partial\Omega} = N r_0^2(\boldsymbol{\epsilon}_i \cdot \boldsymbol{\epsilon}_f)^2 \frac{k_i}{k_f} \sum_{\alpha\beta} c_\alpha c_\beta f_\alpha(Q) f_\beta(Q) S_{\alpha\beta}(Q, \omega). \tag{6}$$

Here $f_\alpha(Q)$ is the atomic form factor for the species α and c_α is the concentration. In the $Q \to 0$ limit, the form factor assumes the value Z_α, the number of electrons of the atom α. In the specific case of vitreous silica, $Z_{Si} = 14$ and $Z_O = 8$, and these values are actually proportional to the atomic masses, $M_{Si} = 28$ and $M_O = 16$. Therefore for vitreous silica, in

the small-Q limit, the scattering cross-section for x-rays becomes proportional to the density–density dynamic structure factor:

$$S_{\rho\rho}(Q,\omega) = \sum_{\alpha\beta} c_\alpha c_\beta \frac{M_\alpha M_\beta}{M_{tot}^2} S_{\alpha\beta}(Q,\omega) \tag{7}$$

and

$$\frac{\partial^2\sigma}{\partial\omega\,\partial\Omega} \propto r_0^2(\boldsymbol{\epsilon}_i \cdot \boldsymbol{\epsilon}_f)^2 \frac{k_i}{k_f} S_{\rho\rho}(Q,\omega). \tag{8}$$

The quantity M_{tot} in equation (7) is the total mass of the unit formula ($M_{tot} = 2M_{\mathrm{O}} + M_{\mathrm{Si}}$ in the present case). The proportionality between the scattering signal and the density–density dynamic structure factor is a peculiarity of vitreous silica and of the IXS techniques (the same does not hold, for example, for neutron scattering, as the thermal neutron scattering lengths are not proportional to the atomic masses). Moreover, the simple relation holds only in the small-Q limit: with increasing Q-value the form factors of oxygen and silicon decrease following different laws, thus invalidating the relation $f_{\mathrm{Si}}(Q)/f_{\mathrm{O}}(Q) \propto M_{\mathrm{Si}}/M_{\mathrm{O}}$.

In conclusion, in the specific case of vitreous silica, the IXS signal at low Q can be well approximated by the density–density dynamic structure factor, but with increasing Q the other components—the charge–charge dynamic structure factor and the cross-terms—start to play a role.

2.2. The IXS beamlines at the European Synchrotron Radiation Facility

All the experiments discussed in this paper were carried out at the very-high-energy-resolution IXS beamlines ID16 and ID28 at the European Synchrotron Radiation Facility (ESRF). The x-ray source is made out of two undulators. The x-ray radiation utilized is the one chosen to optimize the photon flux at the energy used in the experiments. After being pre-monochromatized to a bandwidth of 10^{-4} by a cryogenically cooled Si(1 1 1) double-crystal monochromator, the beam is backscattered by the main monochromator, consisting of a flat, symmetrically cut, silicon crystal oriented along the (1 1 1) direction. The Bragg angle of the monochromator is 89.98°. The family of crystalline planes used by the monochromator has to be chosen as a compromise as regards resolution and output flux requirements; the present experiments were carried at the Si(9 9 9) and Si(11 11 11) reflections ($E = 17\,794$ eV and $E = 21\,748$ eV respectively), which allows overall instrumental energy resolutions of 3.2 and 1.6 meV full width at half-maximum (FWHM) and fluxes of 5×10^9 and 7×10^8 photons on the sample with 200 mA current in the storage ring [27]. The monochromatized beam is focused on the sample by a grazing-incidence toroidal mirror to a spot size of 100 (vertical) × 300 (horizontal) μm^2 FWHM and with a divergence of 40 (vertical) × 120 (horizontal) μrad^2 FWHM. The radiation scattered in the nearly forward direction is analysed by five independent spherical analyser systems, mounted in a row with a constant angular offset of 1.3° on an arm 7 m long. Such an arm covers scattering angles in the range between $\theta_s = 0°$ and 13°. The exchanged wavevector, Q, can be varied accordingly to the relation $Q = 2k_i \sin(\theta_s/2)$. At the two reflections, the angular offset between two neighbouring analysers corresponds to a difference of 2.4° and 3 nm^{-1} in exchanged momentum. Each analyser consists of ≈10 000 small silicon crystals of surface size 0.7×0.7 mm^2 and 3 mm height, glued with ≈10″ tolerance in their relative alignment on a spherical substrate of 6.5 m radius [27]. The analysers operate at the same reflection as the monochromator in the Rowland geometry with 1:1 magnification; each of them collects the radiation scattered at the chosen scattering angle, and focuses it onto a Peltier-cooled, Si-diode detector. The dark counts due to the electronic and environmental noise amount to ≈1 counts min^{-1}. The detector energy resolution is ≈400 eV. Slits in front of

the analysers set the desired momentum resolution, ≈ 0.4 nm^{-1} FWHM in the present cases. The energy scans are performed by varying the monochromator temperature with respect to that of the analyser crystals; the temperature of the main monochromator and analysers is controlled with a precision of ≈ 0.2 mK.

2.3. The experiments

The experiments discussed here were performed on Suprasil vitreous silica samples purchased from Goodfellow. The samples were 2 mm diameter rods, with the cylinder axis orthogonal to the scattering plane. The sample diameter was chosen to be comparable to the x-ray photoabsorption length and to give negligible multiple scattering. The sample quality was tested by measuring its static structure factor $S(Q)$, which was found to be in agreement with previous determinations. The v-SiO_2 rod was placed inside a graphite or tantalum tube, which was resistively heated in vacuum. A 1 mm diameter hole orthogonal to the cylinder axis allowed the passage of the incoming and scattered photons without scattering from the sample heater. The temperature of the sample in the high-temperature experiment was measured with an optical pyrometer.

3. The molecular dynamics simulation

Standard microcanonical MD simulations with periodic boundary conditions were carried out for systems composed of $N = 648$ and $N = 5184$ atoms enclosed in cubic boxes of length $L = 21.39$ Å and $L = 42.78$ Å respectively (mass density $\rho = 2.20$ g cm^{-3}) [17, 18]. We used the two-and-three-body interaction potential proposed by Vashista *et al* [28] which gives, compared with the two-body potentials which are simpler to deal with, a better description of the structural properties of v-SiO_2. The electrostatic long-range interactions were taken into account by the tapered-reaction-field method and the equations of motion were integrated using the leapfrog algorithm with a time step of $\Delta t = 0.5$ fs. A β-cristobalite crystal was melted at 15 000 K and equilibrated for a long time so that the initial crystalline state had no effect on the final configuration. The system was then cooled and thermalized through different states ranging from 5000 K down to 300 K. Two different techniques have been adopted in performing the dynamical study:

(i) the finite-temperature ($T = 1500$ K, 1000 K, 600 K, and 300 K) atomic dynamics of the system in the glassy state was followed by recording instantaneous configurations in different MD runs of 15 ps duration;
(ii) the dynamical matrix (the Hessian of the potential energy function) was calculated for different potential energy minima, reached by a steepest-descent method from the equilibrium configurations [29], and then either diagonalized to obtain a complete set of eigenvalues and eigenvectors or used in the application of the spectral moments method [20, 30].

The reliability of the harmonic approximation is probed by means of the agreement between the NMA (ii) and the MD (i) results at non-zero temperature (300 K). Using MD and NMA, we investigated numerically the x-ray-weighted $S_x(Q, \omega)$ dynamic structure factors for v-SiO_2. As specified above, the presence of two distinct atomic species requires one to calculate the partial dynamic structure factors, which in the classical limits—such as in our MD simulation—can be written as

$$S_{\alpha\beta}(Q, \omega) = \frac{1}{N} \int_{-\infty}^{\infty} \frac{\mathrm{d}t}{2\pi} \, \mathrm{e}^{-\mathrm{i}\omega t} \sum_{ij} \langle \mathrm{e}^{\mathrm{i}\boldsymbol{Q}\cdot\boldsymbol{R}_j^{\alpha}(t)} \mathrm{e}^{-\mathrm{i}\boldsymbol{Q}\cdot\boldsymbol{R}_i^{\beta}(0)} \rangle \tag{9}$$

where the summations over i and j run over all atoms of types α and β respectively and $\boldsymbol{R}_j^\alpha(t)$ is the position vector of atom j at time t. This function can be evaluated directly using the MD atomic trajectories. In the NMA approach, i.e. in the harmonic approximation, one introduces the displacements $\{\boldsymbol{u}_i\}$ from the equilibrium positions $\{\boldsymbol{X}_i\}$, expands the exponential function appearing in equation (9) with respect to $\boldsymbol{Q}\cdot\boldsymbol{u}_i$, and, finally, expands the atomic displacements in terms of the normal modes. Up to the first order in $\boldsymbol{Q}\cdot\boldsymbol{u}_i$, i.e. in the *one-excitation* approximation, one gets $S_{\alpha\beta}(Q,\omega)\approx S^{(0)}_{\alpha\beta}(Q,\omega)+S^{(1)}_{\alpha\beta}(Q,\omega)$, with

$$S^{(0)}_{\alpha\beta}(Q,\omega)=\delta(\omega)\sum_{ij}\mathrm{e}^{-W_{ij}}\mathrm{e}^{-\mathrm{i}\boldsymbol{Q}\cdot(\boldsymbol{X}_j^\beta-\boldsymbol{X}_i^\alpha)}$$
$$S^{(1)}_{\alpha\beta}(Q,\omega)=\frac{k_BT}{\sqrt{M_\alpha M_\beta}}\sum_p\delta(\omega-\omega_p)\frac{1}{\omega^2}\sum_{ij}\mathrm{e}^{-W_{ij}}(\boldsymbol{Q}\cdot\boldsymbol{e}_i(p))(\boldsymbol{Q}\cdot\boldsymbol{e}_j(p))\mathrm{e}^{-\mathrm{i}\boldsymbol{Q}\cdot(\boldsymbol{X}_j^\beta-\boldsymbol{X}_i^\alpha)} \tag{10}$$

where the index p labels the normal modes of the systems, $\{\omega_p\}$ and $\{\boldsymbol{e}_i(p)\}$ are the respective eigenvalues and eigenvectors, and W_{ij} is the Debye–Waller factor exponent. The dynamic structure factor in the harmonic approximation consists of the sum of a δ-function centred at zero frequency and an inelastic contribution. Using equation (10), the x-ray-weighted dynamic structure factor is readily calculated according to equation (7).

In a similar way, from the harmonic approximation of the dynamics and in the 'one-excitation' approximation, one can calculate the current spectra. The longitudinal spectrum is given by

$$C^{(1)}_{L\alpha\beta}(Q,\omega)=\frac{k_BT}{\sqrt{M_\alpha M_\beta}}\sum_p\delta(\omega-\omega_p)\sum_{ij}\mathrm{e}^{-W_{ij}}(\hat{\boldsymbol{Q}}\cdot\boldsymbol{e}_i(p))(\hat{\boldsymbol{Q}}\cdot\boldsymbol{e}_j(p))\mathrm{e}^{-\mathrm{i}\boldsymbol{Q}\cdot(\boldsymbol{X}_j^\beta-\boldsymbol{X}_i^\alpha)} \tag{11}$$

and the transverse spectrum by

$$C^{(1)}_{T\alpha\beta}(Q,\omega)=\frac{k_BT}{\sqrt{M_\alpha M_\beta}}\sum_p\delta(\omega-\omega_p)\sum_{ij}\mathrm{e}^{-W_{ij}}(\hat{\boldsymbol{Q}}\times\boldsymbol{e}_i(p))\cdot(\hat{\boldsymbol{Q}}\times\boldsymbol{e}_j(p))\mathrm{e}^{-\mathrm{i}\boldsymbol{Q}\cdot(\boldsymbol{X}_j^\beta-\boldsymbol{X}_i^\alpha)}. \tag{12}$$

Here the hats indicate unit vectors. The first quantity is simply related to the dynamic structure factor via $C_L(Q,\omega)=\omega^2/Q^2S(Q,\omega)$, while the second one is not directly accessible experimentally in disordered systems.

4. The dynamic structure factor in disorder systems

There is a formally exact procedure for deriving an expression for the dynamic structure factor based on the description of the density-fluctuation correlation function $F(Q,t)=\langle\delta\rho_{\bar{Q}}(t)\,\delta\rho^*_{\bar{Q}}(0)\rangle$, i.e. the frequency Fourier transform of $S(Q,\omega)$, in terms of the generalized Langevin equation [31]:

$$\ddot{F}(Q,t)+\omega_0^2F(Q,t)+\int_0^t m(Q,t-t')\dot{F}(Q,t')\,\mathrm{d}t'=0 \tag{13}$$

where $\omega_0^2=k_BTQ^2/MS(Q)$, $m(Q,t)$ is the 'memory function', and $S(Q)$ is the static structure factor. This equation is 'exact', but all the difficulties associated with the calculation of $F(Q,t)$ are now associated with obtaining $m(Q,t)$. There is, however, an advantage in this formulation: it resides in the fact that—independently of the choice of $m(Q,t)$—the first two

sum rules for $S(Q,\omega)$ are automatically satisfied:

$$\int \mathrm{d}\omega\, S(Q,\omega) = F(Q,t=0) = S(Q)$$
$$\int \mathrm{d}\omega\, \omega^2 S(Q,\omega) = -\ddot{F}(Q,t=0) = \frac{k_B T}{M} Q^2. \tag{14}$$

By Fourier transformation of equation (13), it is easy to show that

$$S(Q,\omega) = \frac{1}{\pi} S(Q) \frac{\omega_0^2 m'(Q,\omega)}{[\omega^2 - \omega_0^2 + \omega m''(Q,\omega)]^2 + [\omega m'(Q,\omega)]^2} \tag{15}$$

where $m'(Q,\omega)$ and $m''(Q,\omega)$ are the real and imaginary parts of the time Fourier transform of the memory function. In the $\omega\tau_\alpha \gg 1$ limit, a limit that is certainly reached in the case of glassy samples, the memory function can be considered as the sum of two contributions: a constant—which reflects the frozen α-process—plus a very fast decay in a short time. The latter contribution to the memory function—often referred to as a 'microscopic' or 'instantaneous' process—is usually represented as a delta function. Introducing the two parameters $2\Gamma(Q)$ and $\Delta^2(Q)$ which represent respectively the areas of the 'instantaneous' process and the long-time limit of $m(Q,t)$, the memory function is approximated by

$$m(Q,t) = 2\Gamma(Q)\delta(t) + \Delta_\alpha^2(Q) \tag{16}$$

and therefore, using equation (15), $S(Q,\omega)$ reduces to

$$S(Q,\omega) = S(Q)\left[f_Q \delta(\omega) + (1 - f_Q)\frac{1}{\pi} \frac{\Omega^2(Q)\Gamma(Q)}{(\omega^2 - \Omega^2(Q))^2 + \omega^2\Gamma^2(Q)} \right] \tag{17}$$

where

$$\Omega(Q) = \sqrt{\Delta_\alpha^2(Q) + \omega_0^2} \qquad f_Q = 1 - \omega_0^2/\Omega^2(Q).$$

This expression is the sum of an elastic line (the frozen α-process) and an inelastic feature which is formally identical to a damped harmonic oscillator (DHO) function; the central line accounts for a fraction f_Q—the Debye–Waller or non-ergodicity factor—of the total intensity.

Recently it has been shown via MD [25] that the 'microscopic' contribution to the memory function cannot be represented by a delta function. There are, indeed, clear indications that this 'microscopic' part is responsible for a positive dispersion of the sound velocity in 'harmonic' model glasses [25], and is responsible for the majority of the positive dispersion of the sound velocity in liquids [32]. The simplest generalization of the delta function appearing in equation (16) considers a Debye-like 'microscopic' contribution to the memory function:

$$m(Q,t) = \Delta_\mu^2(Q)\mathrm{e}^{-t/\tau_\mu} + \Delta_\alpha^2(Q). \tag{18}$$

The quantity τ_μ entering in this equation is the characteristic time of the 'microscopic' contribution to the memory function. Obviously, whenever $\Omega\tau_\mu \ll 1$, equation (18) produces for $S(Q,\omega)$ a DHO-like lineshape with

$$\Omega(Q) = \sqrt{\Delta_\alpha^2(Q) + \omega_0^2} \qquad \Gamma(Q) = \Delta_\mu^2(Q)\tau_\mu.$$

In the past, in analysing the IXS spectra of glasses, the simplified DHO expression for $S(Q,\omega)$ has been used; no systematic deviation of the experimental data from the fitting lineshape was noticed. In the following we will adopt equation (17) as the fitting function.

It is worth noting that—despite the fact that $m(Q,t)$ is usually referred to as the 'generalized viscosity'—the origin of the microscopic contribution to the memory function is not necessarily a 'viscous' process. On the contrary, as shown in reference [25], a microscopic part of $m(Q,t)$ has been found through MD in harmonic model glasses also, thus

indicating that the origin of such a contribution—mainly responsible for the high-frequency sound attenuation—cannot be related to dynamic processes (such as viscous damping or anharmonicity).

5. Results and discussion

5.1. Qualitative observation of Brillouin peaks in v-SiO_2

To illustrate the main features of the IXS signal, in figure 1 we report two spectra taken at $Q = 1$ and 2 nm^{-1} for vitreous SiO_2 at $T = 1075$ K [3]. In figure 1(A), the total spectra are compared with the experimentally determined resolution function, which has been aligned with the dominant peak centred at zero energy transfer (elastic peak). This peak—as discussed before—is due to the frozen density fluctuations existing in glasses at all Q-values, and its broadening is due to the finite energy resolution. On both sides of this elastic peak, one observes the presence of inelastic features, emphasized in the insets. The difference spectra, obtained by subtracting the central peak represented by the resolution function from the data, are reported in figure 1(B) in order to highlight the Q-dependence of the inelastic signal. One can observe that the average energy position and width of this signal increase with increasing Q. In particular, the two arrows show that the energy position doubles on doubling the Q-value. This behaviour is the one expected for propagating excitations, dispersing with a linear

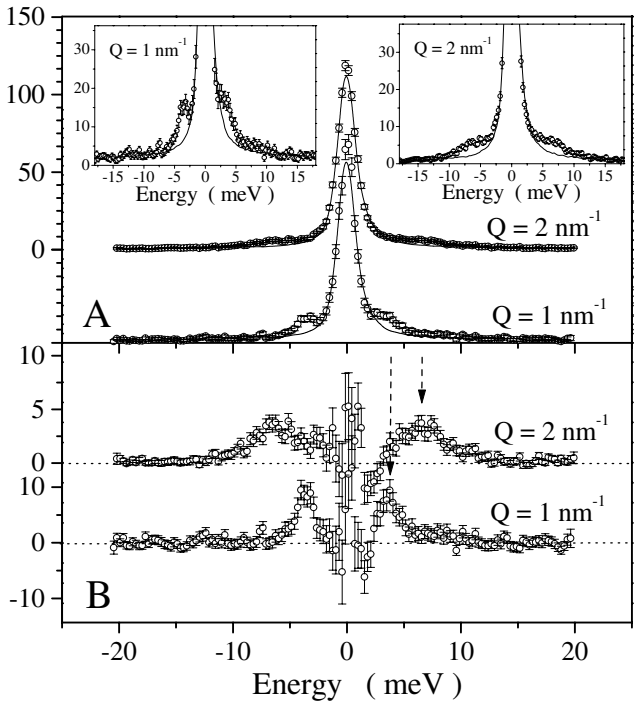

Figure 1. (A) IXS spectra (○) of vitreous silica taken at $T = 1075$ K at $Q = 1$ and 2 nm^{-1}, with total integration times of 415 and 800 s, respectively. The full lines are the measured resolution functions, which have been aligned and scaled to the central peak. The two insets are present to emphasize the inelastic signal on either side of the central peak. (B) Difference spectra, obtained by the subtraction of the scaled resolution function from the spectra reported in (A). The arrows indicate the inelastic peak energy positions, which scale approximately with the Q-transfer.

relation. This qualitative result has been found to be a general feature of all the liquids and glasses investigated so far in the Q-region below ≈ 5 nm^{-1}.

This qualitative procedure has the advantage of showing important behaviours without invoking specific models. Obviously, however, the *difference* spectra of figure 1(B), derived from the *measured* spectra of figure 1(A), contain a *high degree of arbitrariness*. Indeed, as the central peak is much more intense than the inelastic signal—by a factor of ≈ 20 in the present case—a small modification of the (unknown!) factor that is used to scale the intensity of the resolution function to that of the elastic peak in the IXS spectrum strongly modifies aspects of the difference signal, especially at low energy transfer. As an example, in figure 1 the normalization factor has been chosen in such a way as to force the inelastic signal to vanish at $\omega = 0$, but there are no theoretical reasons or experimental evidence for such a behaviour. It is clear that the 'subtraction' procedure presented cannot be used to draw any quantitative conclusions regarding the features of the inelastic signal, and a more detailed fitting procedure is needed[4].

5.2. *Fits of the IXS data using the DHO model*

The remainder of this paper will use the procedure developed in section 4 and adopted in previous published works [4, 13]. In fact we will present the results obtained by fitting the experimental data to the previously derived model (equation (17)) convoluted with the experimentally determined resolution function. The model in equation (17), however, does not take into account the quantum nature of the systems investigated (which shows up mainly in the asymmetry of the Brillouin peaks according to the detailed-balance principle). In order to provide a fitting function with the proper frequency asymmetry, the following scheme is often adopted:

$$S_q(Q,\omega) = \frac{\hbar\omega}{k_B T}[n(\omega)+1]S(Q,\omega) \tag{19}$$

where $S_q(Q,\omega)$ is the 'quantum' dynamic structure factor utilized to fit the spectra, $S(Q,\omega)$ is the 'classic' (symmetric) dynamic structure factor, and $n(\omega)$ is the Bose population factor. With this choice, obviously,

$$S_q(Q,\omega) = \exp(\hbar\omega/k_B T)S_q(Q,-\omega) \qquad \lim_{\omega\to 0} S_q(Q,\omega) = S(Q,\omega).$$

As a representative example of the fitting procedure, the inelastic x-ray scattering spectrum of v-SiO_2 at $T = 1375$ K and $Q = 1$ nm^{-1} is reported in figure 2 together with its best fit. A standard χ^2-minimization procedure has been utilized to determine the relevant fitting parameters, namely the excitation energy $\Omega(Q)$, the excitation width $\Gamma(Q)$, and the elastic-to-inelastic intensity ratio (or non-ergodicity factor, or Debye–Waller factor) f_Q. The spectrum (open circles) is dominated by an intense elastic peak, whose shape is determined by the instrumental resolution function (dotted line), of FWHM = 1.6 meV in the present case. At the sides of the central peak, well above the tails of the elastic scattering broadened by the resolution function, the inelastic signal is clearly visible. The fitting function is reported as a full line, and it agrees very well with the IXS data. Also shown in figure 2 are the individual (elastic and inelastic) contributions to the fitting function. The bottom panel of figure 2 shows a close-up of the region where the inelastic intensity is more visible, while the middle panel shows the residual of the fit reported in units of the standard deviation. The observed inelastic signal is due to collective density fluctuations, and it is observed to change with Q at the Q-points investigated.

[4] The procedure of subtracting the elastic peak from the spectra with an arbitrary normalization factor has been used in reference [11] to establish the validity of a specific model that predicts vanishing intensity at zero frequency.

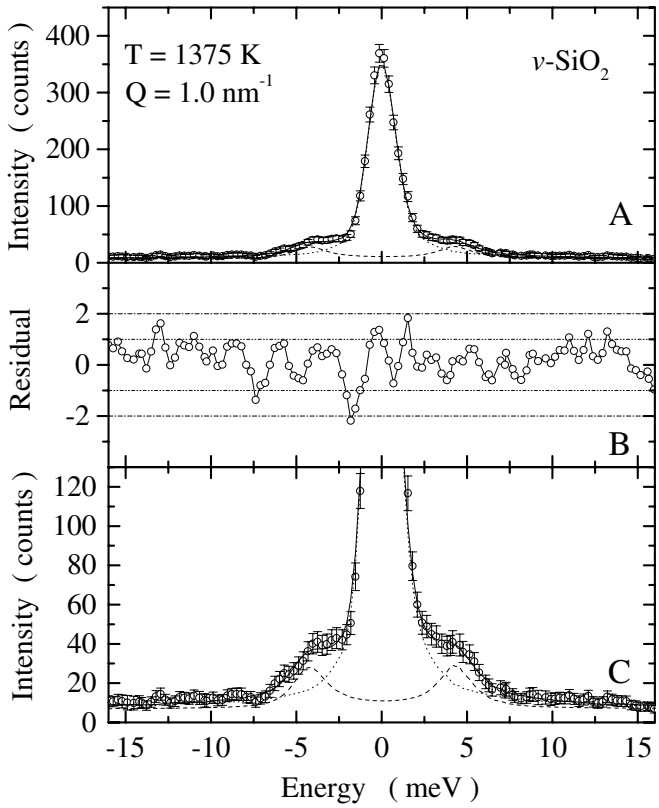

Figure 2. (A) X-ray spectra of v-SiO_2 at $T = 1375$ K and $Q = 1$ nm^{-1}. The data are shown together with their best fits (full line) and the individual contributions to the fitting function: the elastic peak (dashed line) and inelastic components (dotted line). (B) The residual (in units of σ) of the fit. (C) As (A), but with an expanded vertical scale, used to emphasize the inelastic contribution to the spectrum.

The inelastic x-ray scattering spectra taken at $T = 1100$ K in the $1 \leqslant Q \leqslant 4$ nm^{-1} region are shown in figure 3. These were the first IXS measurements to be made on v-SiO_2, and, unlike the case for figure 1 and 2, they were measured with an energy resolution of 3.2 meV. The dashed lines represent the resolution functions, and are aligned and scaled to the central peak in each spectrum. As seen from the theoretical fitting function for the inelastic contribution to the dynamic structure factor, the excitations are characterized by a clear Q-dependence.

As further examples of IXS spectra, in figure 4 we report the temperature dependence of the spectra at the fixed exchanged momentum $Q = 1.6$ nm^{-1} [10]. This study was performed to link the observed excitations to the anomalous non-Debye behaviour of the density of states (DOS) in this glass. The main anomaly is an excess of states at $E \approx 5$ meV, and this gives rise to a feature in the DOS referred to as the boson peak (BP). The IXS spectra were collected at a Q-value chosen such that—at room temperature—the corresponding excitation energies are in the range of the boson peak energy. It is possible to observe directly from the raw data in figure 4 that, in addition to the expected increase of intensity with T, there is also a mild T-dependence of the excitation energy. This dependence is emphasized in the inset of figure 4, where $\Omega(Q, T)$ is reported versus T. A T-dependence of the sound velocity was also observed in low-frequency measurements, but it is much more evident in the high-frequency region

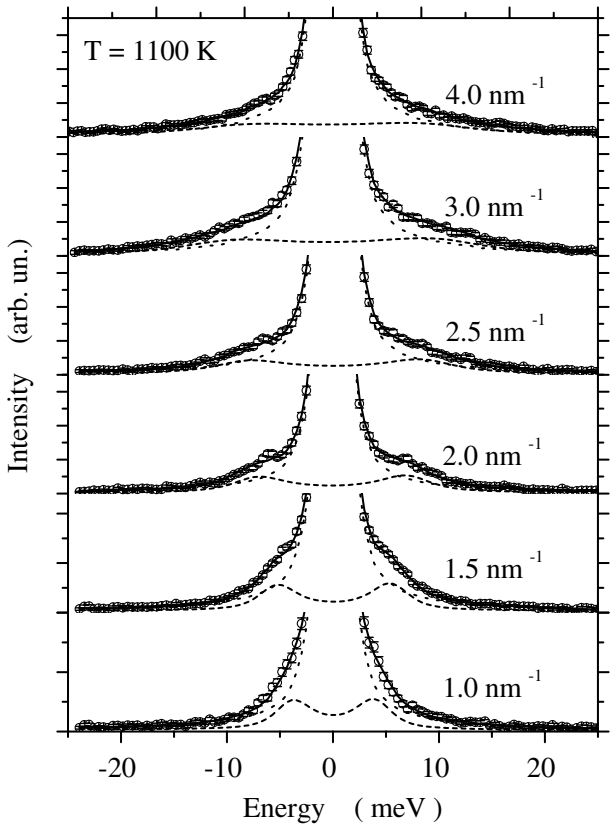

Figure 3. X-ray spectra of v-SiO_2 at $T = 1100$ K taken at different Q-values. The data are shown together with their best fits (full lines) and the individual contributions to the fitting function: the elastic peak (dashed lines) and inelastic components (dotted lines).

examined here. This difference in T-dependence of the low- and high-Q excitation regimes indicates a temperature deformation of the acoustic mode dispersion relation. Moreover, the comparison between $\Omega(Q, T)$ and the T-behaviour of the boson peak position has provided a strong indication that the vibrations probed by IXS contribute to the BP [10].

Let us now turn our attention to the dependence of the parameters extracted from the fits. A summary of the Q-dependence of $\Omega(Q)$, at the different measurement temperatures, is reported in figure 5 for $Q \leqslant 4$ nm^{-1}. It is possible to observe an almost linear dispersion with Q, which starts to bend downwards with increasing Q-value. The small temperature dependence of the excitation energy at fixed Q—emphasized in figure 4—is here masked by the error bars.

The Q-dependence of the other relevant parameter, $\Gamma(Q)$, is reported in figure 6 using a log–log scale (full squares in the main figure; full diamonds, squares, and triangles in the inset) together with those determined using other techniques [15]. The full line represents the best fit to $\Gamma(Q)$ determined by means of IXS, and has a slope of 1.95, thus indicating that $\Gamma(Q) \propto Q^2$ over the whole IXS Q-range examined. This Q^2-behaviour is consistent with low-Q picosecond optical technique (POT) acoustic attenuation measurements on v-SiO_2 at room temperature [33]. The consistency between the IXS data, taken at $T = 300$, 1100, and 1375 K and at $Q \geqslant 1$ nm^{-1}, and the data of reference [33], taken at $T = 300$ K and at

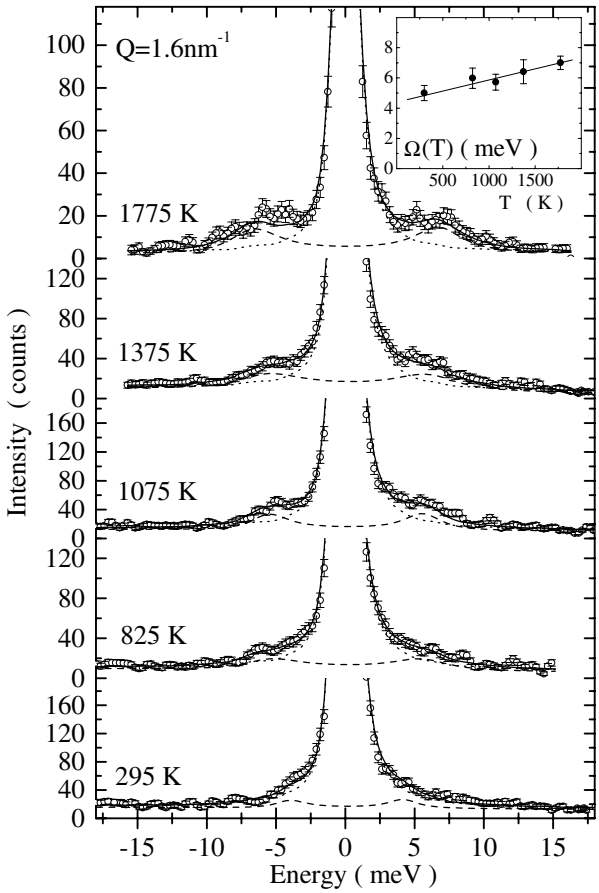

Figure 4. X-ray spectra of v-SiO_2 at $Q = 1.6$ nm^{-1} taken at different temperatures. The data are shown together with their best fits (full lines) and the individual contributions to the fitting function: the elastic peak (dotted lines) and inelastic components (dashed lines). In the inset we report the excitation energy, $\Omega(T)$, derived from the DHO model. The full line is a linear fit.

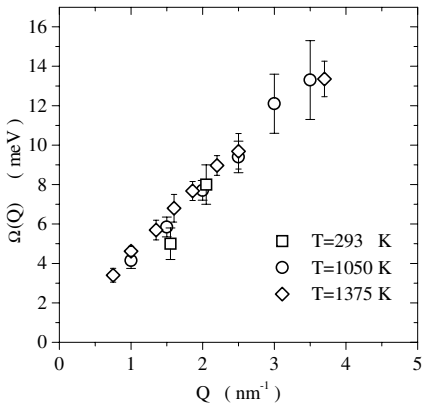

Figure 5. The Q-dependence of the excitation energies determined from the fits to the IXS spectra of vitreous silica at different temperatures: $T = 293$ K (squares), $T = 1050$ K (circles), $T = 1375$ K (diamonds).

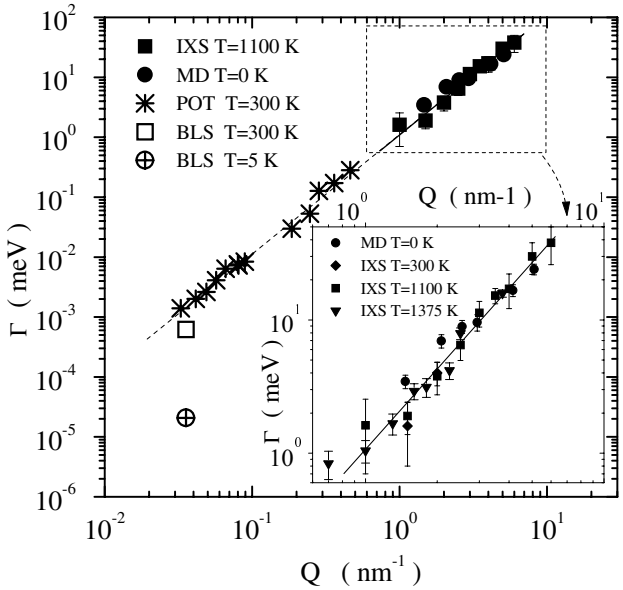

Figure 6. The parameters $\Gamma(Q)$ as a function of Q at the temperatures indicated in the IXS (full squares) and BLS (open squares) Q-regions. Data from MD simulation (full circles) and from the POT (stars) are also reported. The inset shows an enlargement of the high-Q region. The full line represents $Q^{1.95}$-behaviour, which is the best fit to $\Gamma(Q)$ at high Q. Also shown in the figure are extrapolations of the $Q^{1.95}$-law in the low-Q range (thin full line) and the $Q^{2.6}$-dependence (dashed line) indicated by the low-T BLS data.

Q-values an order of magnitude smaller, is in fact excellent. This behaviour indicates that: (i) the Q^2-dependence of Γ is genuine; and (ii) there is no visible temperature dependence of the linewidths of the excitations in the range between room temperature and 1375 K in this high-Q region.

There is, however, a significant inconsistency between the extrapolation of $\Gamma(Q)$ at low Q and the values measured using BLS [34]. This fact, together with the strong T-dependence observed below $\approx$100 K in the BLS determination of $\Gamma(Q)$ (see figure 7), leaves open the question of the existence in vitreous silica of a 'fast' relaxation process influencing the collective excitations in the GHz range and below.

The Q^2-dependence of $\Gamma(Q)$ in the high-Q region, together with the linear dependence of $\Omega(Q)$, naturally leads to the existence of a specific Q-value, $Q = Q_m$, where the condition $\Gamma(Q) = \Omega(Q)$ is fulfilled. This condition can be interpreted as the point in the dispersion relation describing the transition of the collective dynamics from a propagating longitudinal acoustic regime to excitations that are still spatially extended but no longer propagating. In vitreous silica this threshold is found at $Q_m \approx 3.5$ nm^{-1} ($E \approx 10$ meV). Obviously this Q-point does not mark a sharp transition in the character of the modes, but locates a region in Q-space where a continuous fading out of the propagating character takes place.

5.3. Comparison among DHO and effective-medium approximation models for v-SiO_2

The picture discussed earlier casts vitreous silica in the same phenomenology as was identified by means of IXS for the other glasses investigated so far. This picture, together with its theoretical background, has been criticized in references [5, 7]. There, the analysis of the

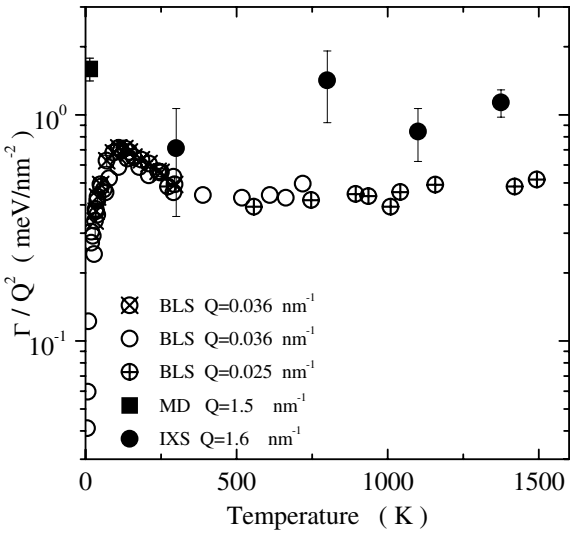

Figure 7. The temperature dependence of Γ_Q/Q^2. The open symbols refer to BLS data at $Q \approx 0.036\,\mathrm{nm}^{-1}$ (○ and ⊗) and $Q \approx 0.025\,\mathrm{nm}^{-1}$ (⊕), the full circles to IXS data at $Q = 1.6\,\mathrm{nm}^{-1}$, and the full squares to MD simulations in the harmonic ($T = 0$ K) limit.

IXS spectra of vitreous silica has been performed using a different model for $S(Q, \omega)$—the so-called effective-medium approximation (EMA) model—that assumes the existence of a threshold frequency (ω_{co}) between propagation and localization of the collective modes. This crossover takes place as a consequence of the strong elastic scattering of the excitations from inhomogeneity in the glassy structure. Accordingly, the Q-behaviour of $\Gamma(Q)$ is expected to be $\Gamma(Q) \propto Q^4$. Unfortunately, the differences between the $S(Q, \omega)$ lineshape predicted by the EMA model and by the generalized Langevin equation with the instantaneous memory function approximation (equation (17)) are substantial only at low frequency. Here the EMA $S(Q, \omega)$ vanishes in the $\omega \to 0$ limit while the DHO one reaches, in the same limit, a finite value. The presence of the intense elastic peak in the experimental data, however, has so far prevented discrimination between the two models. These issues have been investigated further using two different approaches. The first one takes advantage of MD data to simulate the spectra. This allows one to circumvent the elastic peak problem. The second one takes advantage of an experimental protocol consisting of measuring $S(Q, \omega)$ at constant ω rather than at constant Q. This gives spectra where the effect of the elastic signal appears as an almost flat background below the Brillouin peaks. We first discuss the outcome of the MD simulation of vitreous silica.

As a first step, in order to show the reliability of the numerical simulation as regards representing—at least at a qualitative level—the dynamic structure factor of vitreous silica, we report in figure 8 the comparison of an INS determination of $S(Q, \omega)$ (open circles) with the neutron-weighted dynamic structure factor $S_n(Q, E)$ calculated by MD simulation at the same temperature. Both the simulation [18] and the experiment [35] were performed at $T \approx 1100$ K and at a constant energy $E = 5.4$ meV, corresponding to the position of the boson. The comparison is satisfactory, and indicates the ability of the potential model adopted (see section 3) to represent the high-frequency dynamics of vitreous silica. Having confidence in the MD results, we have calculated the longitudinal current spectra $C_L(Q, \omega)$ and compared them with the predictions of the two models proposed to interpret the experimental data. The

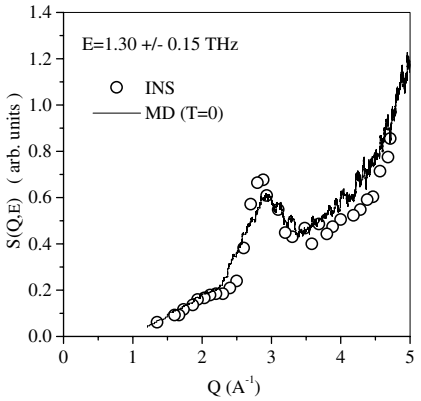

Figure 8. The Q-dependence of the inelastic neutron scattering from vitreous silica at the fixed energy of 1.3 THz. The circles represent the data of reference [35] at $T = 1104$ K; the full line shows the MD calculation in the harmonic limit from reference [18].

calculated quantity is the spectrum of the current $C_L(Q, \omega)$ and not the dynamic structure factor, for two reasons:

(i) the excitation frequency can be derived from the current spectra without any fitting procedure (it is directly the maximum of the current spectra); and
(ii) the transverse current spectrum can also be calculated, thus giving important information on the whole acoustic-like dynamics, as discussed below.

We show in figure 9, as an example, the longitudinal current spectrum at $Q = 2.08$ nm^{-1}. This is reported together with its best fit to the DHO model (see equation (17), full line) and to the EMA model (reference [5], dashed line). The agreement favours the DHO model,

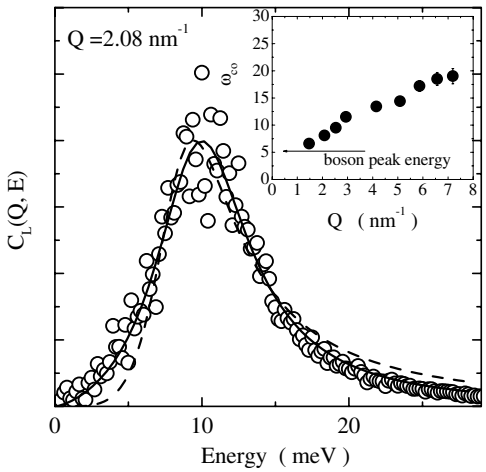

Figure 9. Am example of a longitudinal current spectrum (at $Q = 2.08$ nm^{-1}) calculated by means of NMA (harmonic approximation) in reference [18] (open circles). The full and dashed lines represent the best fit to the simulation data using the DHO and the EMA models respectively. In the inset we report the Q-dependence of the crossover frequency ω_{co}, one of the parameters of the EMA model.

especially in the contentious low-frequency region. Moreover, in the case of the EMA model, reliable fits can be obtained just leaving the ω_{co}-parameter free to vary for different Q-values. In fact, as reported in the inset of figure 9, the crossover frequency ω_{co}, that according to the localization model should be Q-independent, is found to be strongly Q-dependent. Moreover, this parameter, that should indicate the localization edge and is expected to coincide with the boson peak energy, assumes values that are always higher than the energy of the boson peak. These two significant contradictions seem to favour the theoretical approach based on the DHO for modelling $S(Q, \omega)$ for vitreous silica in the Q-range considered.

The MD longitudinal current spectrum allows one to determine the parameter $\Omega(Q)$—derived from the current maxima—and $\Gamma(Q)$—derived from a fit to equation (17). These parameters are compared to the experimental ones in figures 6 and 7. The data for $\Gamma(Q)$ are also shown on a linear scale in figure 10. One can observe a quantitative agreement, and, in particular, the $\Gamma(Q)$ values compare very well with those measured by means of IXS for temperatures ranging from $T = 300$ to 1050 K: both sets of values show a $\Gamma(Q) \propto Q^2$ behaviour. Let us recall that the current spectra have been calculated in the harmonic approximation, i.e. according to equation (10). Therefore, the agreement of the $\Gamma(Q)$ values found in the harmonic approximation with those measured in the real system strongly indicates that the excitation broadening, in the Q-range investigated, is related to the structural disorder rather than to anharmonicity, viscous damping, or other dynamical effects.

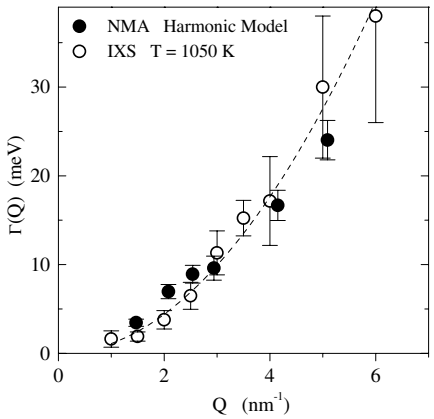

Figure 10. The Q-dependence of the excitation broadening $\Gamma(Q)$ derived from the fit of the DHO model to the NMA current spectra (full circles) compared to the IXS data at $T = 1050$ K (open circles).

The second route followed to discriminate between the two models gives *direct experimental evidence* on the existence for well defined Brillouin peaks in the IXS spectra of amorphous silica at energies above the boson peak energy. In contrast to the approach taken in the earlier discussion of the IXS experiments [5, 6, 9–11], where the spectra were measured at constant Q and as a function of energy, now we discuss constant-ω cuts of $S(Q, \omega)$ taken as a function of Q [12]. To appreciate the advantage of this approach, we recall that in the constant-Q spectra, as a consequence of the finite energy resolution, the elastic component gives rise to a tail $\sim\omega^{-2}$ whose intensity in the Brillouin peak energy region is often stronger than that of the peak itself. Therefore, the extraction of the spectroscopic parameters of the Brillouin peak necessarily requires a fitting procedure and the assumption of a model function for $S(Q, \omega)$. In contrast, in the constant-ω measurements, the elastic contribution convoluted with the instrumental response function gives rise to an almost Q-independent background

which should not significantly affect the position and lineshape of the inelastic signal. This approach allowed us to demonstrate the presence of a Brillouin peak at an energy larger than E_{BP}, as seen in figure 11 where the 'inelastic' contributions to $S(Q, \omega = \text{constant})$—derived according to the procedure illustrate in reference [12]—are reported at selected constant ω-values. Therefore, without any specific model for $S(Q, \omega)$, these measurements demonstrated that the boson peak cannot mark the transition between propagating and localized dynamics in vitreous silica.

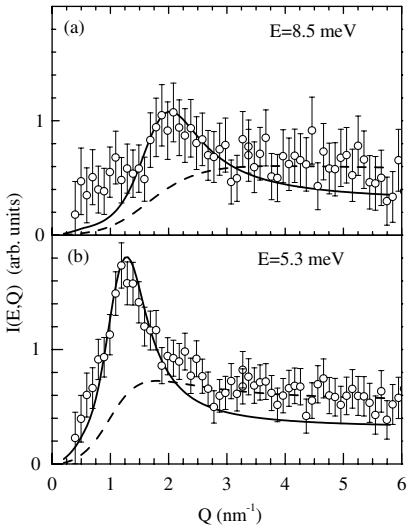

Figure 11. The inelastic contributions to the constant-E IXS spectra (circles) are reported together with their error bars as a function of Q for two energies: (a) $E = 8.5$ meV; (b) $E = 5.3$ meV. The full (dashed) lines are the parameter-free lineshapes calculated via the DHO and EMA models. The numerical values of the parameters entering these functions are taken from references [6] and [5] respectively. The two theoretical predictions have been multiplied by arbitrary scale factors.

In figure 11 we also report, as solid and dashed lines, the inelastic parts of $S(Q, \omega)$ obtained from equations (17) and the EMA model respectively. Both models have been convoluted with the experimental resolution function. In calculating the theoretical expressions for $S(Q, \omega)$ we have used the values of the parameters reported in references [6] and [5] respectively. The only adjustable parameter is an intensity factor, which has been chosen arbitrarily. As can be seen, the DHO model is in good agreement with both constant-ω spectra, where it accounts for the presence of the Brillouin peak and the high-Q plateau, although the relative intensity of these two main features is not completely reproduced. In contrast, the EMA model fails to reproduce the existence of the observed Brillouin peak. This is not surprising, as the EMA model is based on the assumption that at $\approx$5 meV (the BP energy) the vibrational modes in vitreous silica become localized. This analysis further confirms the conclusions obtained using the MD data.

5.4. High-Q behaviour and transverse dynamics

Another issue, becoming increasingly important, is the observation of an inelastic signal at 'high' Q-values, i.e. around and above the first sharp diffraction peak located, in vitreous silica, at $Q \approx 22$ nm^{-1}. This signal has already been observed for v-SiO_2 in INS (see for example reference [5]), and it is clearly visible also in the constant-Q IXS spectra, as exemplified in

figure 12. In these spectra, in fact, the inelastic signal at high Q has a large intensity, as compared to the Brillouin peak, and a behaviour distinctly different from the dispersing trend of the longitudinal acoustic excitations. It is worth noting that such inelastic intensity has already been observed by means of IXS, MD simulations, and theoretical predictions in the constant-Q cuts of $S(Q, \omega)$ for other glassy systems. On the theoretical side, the application of the MCT formalism to the glassy phase allowed identification of the presence of one (or two) secondary features (named the anomalous oscillatory peak—AOP—and/or oscillatory peak—OP) in $S(Q, \omega)$ for hard-sphere [1] and rigid dipolar hard-sphere [36] systems. In [1] and [36] these AOPs and/or OPs have been related to the boson peak. On the experimental side, these secondary features have been clearly detected in liquid water and—by comparison to the spectra of crystalline ice Ih—these have been ascribed to the transverse dynamics. This interpretation has been confirmed by a subsequent MD simulation of liquid water [37]. In the case of vitreous silica, the secondary feature has an almost Q-independent shape, and is 'peaked'[5] around 5 meV (i.e. close to the boson peak energy). Its intensity increases with increasing Q. Similarly to the case for liquid water [37], one can identify its origin by taking advantage of the MD results, and in particular of the possibility of calculating the *transverse* current spectra.

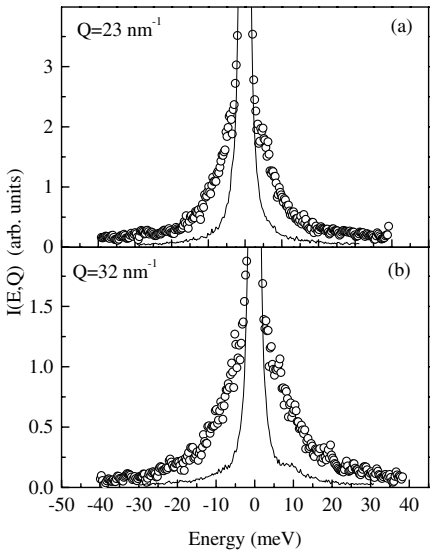

Figure 12. IXS spectra of v-SiO_2 at $T = 1200$ K taken at constant Q (circles) at large Q-values: (a) $Q = 23$ nm^{-1} and (b) $Q = 32$ nm^{-1}. The full lines are the resolution functions aligned with the elastic peaks.

In figures 13 and 14 we report the longitudinal (full lines) and transverse (dashed lines) current spectra at selected Q-values in the regions of 'small' ($Q < 8$ nm^{-1}) and 'high' ($Q > 8$ nm^{-1}) Q respectively.

These spectra have been calculated—see reference [17]—in the harmonic and in the one-excitation approximations according to equations (11), (12), and (7). These figures appear very similar to those calculated by Horbach *et al* at finite temperature and with a different interaction potential model [19]. Both $C_L(Q, \omega)$ and $C_T(Q, \omega)$ show the existence of two excitations

[5] Strictly speaking it is not possible to identify a 'peak' frequency, as the inelastic signal appears to be a broad band extending from low frequency (where the strong elastic line prevents identification of its shape) up to ≈10 meV.

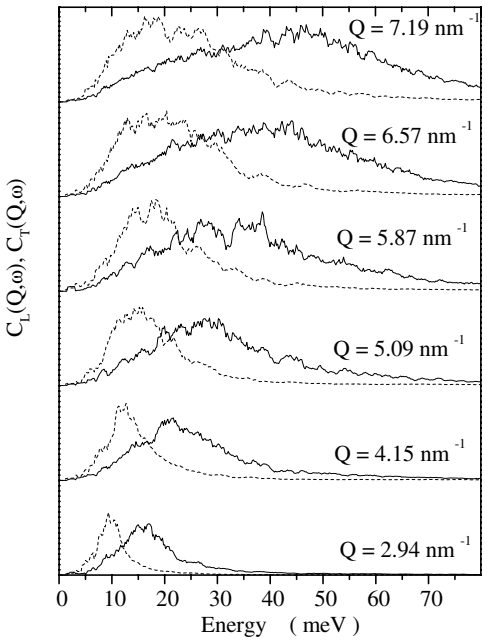

Figure 13. Longitudinal (full lines) and transverse (dashed lines) current spectra obtained by NMA at the 'small' Q-values indicated, from reference [17].

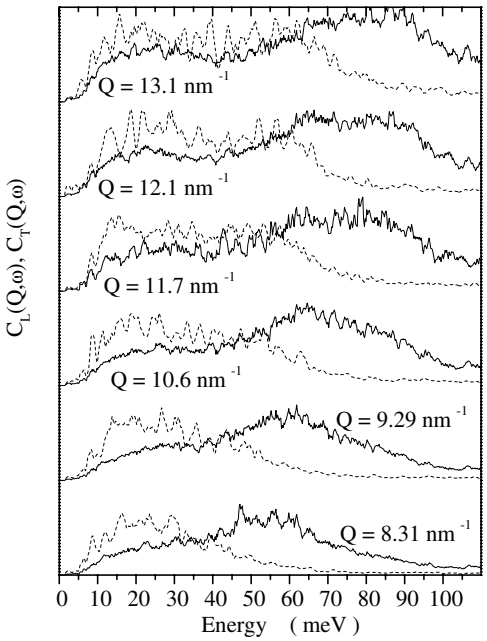

Figure 14. Longitudinal (full lines) and transverse (dashed lines) current spectra obtained by NMA at the 'high' Q-values indicated, from reference [17].

which become clearer and clearer with increasing Q. The high-frequency excitation disperses with Q and appears at each Q-value in the longitudinal current spectra, while it shows up as a bump in the transverse current spectra only at $Q > 10$ nm^{-1}. This feature, obviously, corresponds to the (quasi-) longitudinal sound branch discussed before.

The behaviour of the low-frequency excitation is in some sense opposite: it is always present in the transverse current spectra, while it appears in the longitudinal current spectra only at $Q > 8$ nm^{-1}. At small Q, the low-frequency peak disperses with a sound velocity of $\approx$3800 m s^{-1} and becomes almost non-dispersing at $Q > 10$ nm^{-1}. (Let us call this low-frequency feature—which is the main feature in the transverse current spectra and the secondary feature in the longitudinal current spectra—the transverse mode.) Consequently, the transverse current data provide grounds for interpreting the low-frequency intensity observed in the INS and IXS experiments at high Q-values as due to this transverse dynamics. In fact, the behaviour of the experimental data is fully consistent with the phenomenology associated with the secondary feature in the MD longitudinal current spectra.

The possibility of observing the transverse dynamics in the longitudinal current spectra, both in MD simulations and in the experiments, comes from the feature that the polarization character of the modes in a disordered system is well defined only in the long-wavelength limit. In contrast it is ill defined at short wavelengths, especially in the limit where the wavelength is comparable to the scale of the topological disorder. In this limit it is no longer possible to define a 'pure' transverse or longitudinal excitation. This explains why one can observe the transverse dynamics in longitudinal spectra better with increasing Q-value. Consequently, on the strength of this observation and thanks to the MD simulation, one can safely conclude that the signal observed in $S(Q, \omega)$ at $\approx$5 meV at Q larger than 10 nm^{-1} by means of INS [5] and IXS [12, 38] is associated with the transverse acoustic branch.

This assignment has a further important implication. We notice that in the large-Q limit, the transverse branch loses all dispersion character and, in the current spectra, is centred at an energy of ≈20 meV (see figure 15). Moreover, in $S(Q, \omega)$, its broadening becomes comparable to its energy position ($E \approx 5$ meV). Consequently, one expects the density of vibrational states associated with these modes to possibly show up as a bump at an energy very close to that where this excitation is seen in the *dynamic structure factor*, i.e. at ≈5 meV. This energy corresponds in fact to the location of the boson peak. Therefore, in this picture, the boson peak should not be associated with the end of the longitudinal branch but with the high-frequency limit of the transverse dynamics. This picture is in agreement with a recent theoretical work by Taraskin *et al* which associates the boson peak with the glassy counterpart of the lowest-frequency Van Hove singularity of the corresponding crystalline structure, which in SiO_2 is due to the transverse dynamics [22].

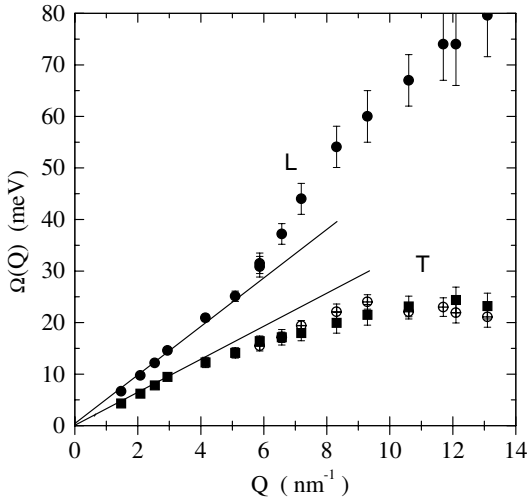

Figure 15. Positions of the maxima of the longitudinal (full circles) and of the transverse (full squares) current spectra. The crossed circles show the position of the second peak appearing—at high Q—at frequency smaller than that of the main peak in the longitudinal current spectrum.

6. Conclusions

The analysis presented in this work summarizes the contribution of the IXS technique in the study of the high-frequency dynamics of vitreous silica. The IXS work is put into perspective with the contributions of other experimental tools such as INS, BLS and the POT, and of numerical and theoretical methods. We also summarize the present understanding of the transition of the collective dynamics from a propagating to a non-propagating regime in this glass. In this respect, a theoretical framework based on the general formalism of the Langevin equation gives an account of the experimental findings, and shows that the sound attenuation in the high-frequency limit considered is determined by the topological disorder. Finally, study of the inelastic signal at high Q-values suggests that the boson peak is related to the high-Q limit of the transverse dynamics. It is our opinion that the results reviewed here for vitreous silica bear many general features that should be present for other glasses. This provides strong motivation to continue the combined investigation by means of IXS and other well established methods of the high-frequency collective dynamics of topologically disordered materials.

Acknowledgments

The IXS work presented here was possible thanks to collaboration with P Benassi, S Caponi, A Cunsolo, A Fontana, M Krisch, C Masciovecchio, V Mazzacurati, A Mermet, G Monaco, M Montagna, O Pilla, F Rossi, M Sampoli, T Scopigno, G Signorelli, R Verbeni, G Viliani. We thank R Dell'Anna for providing the simulation data reported here which are part of her PhD thesis work. We also benefited from discussions with U Balucani, L Borjesson, U Buchenau, E Duval, B Frick, A Matic, M Nardone, F Sciortino, A Sokolov.

We would also like to acknowledge those who contributed to the development of the new IXS spectroscopic tool on the ID16 and ID28 beamlines at the ESRF. In particular, the construction and operation of the beamlines is possible thanks to the technical help of D Gambetti, B Gorges, C Henriquet, K Martel and J F Ribois from the ESRF, and O Consorte and W Galli from the Brillouin Spectroscopy Group of the University of L'Aquila.

References

[1] Goetze W and Mayr M R 2000 *Phys. Rev.* E **61** 587
[2] Martin-Mayor V, Mezard M, Parisi G and Verrocchio P 2001 *J. Chem. Phys.* **114** 8068
[3] Sette F, Krisch M, Masciovecchio C, Ruocco G and Monaco G 1998 *Science* **280** 1550
[4] Masciovecchio C, Ruocco G, Sette F, Krisch M, Verbeni R, Bergmann U and Soltwisch M 1996 *Phys. Rev. Lett.* **76** 3356
Masciovecchio C, Monaco G, Ruocco G, Sette F and Soltwisch M 1998 *Phil. Mag.* **77** 533
Masciovecchio C, Monaco G, Ruocco G, Sette F, Cunsolo A, Krisch M, Mermet A, Soltwisch M and Verbeni R 1998 *Phys. Rev. Lett.* **80** 544
Mermet A, Cunsolo A, Duval E, Krisch M, Masciovecchio C, Perghem S, Ruocco G, Sette F, Verbeni R and Viliani G 1998 *Phys. Rev. Lett.* **80** 4205
Monaco G, Fioretto D, Masciovecchio C, Ruocco G and Sette F 1999 *Phys. Rev. Lett.* **82** 1776
Fioretto D, Buchenau U, Comez L, Sokolov A, Masciovecchio C, Mermet A, Ruocco G, Sette F, Willner L, Frick B, Richter D and Verdini L 1999 *Phys. Rev.* E **59** 4470
Fontana A, Dell'Anna R, Montagna M, Rossi F, Viliani G, Ruocco G, Sampoli M, Buchenau U and Wischnewski A 1999 *Europhys. Lett.* **47** 56
Sokolov A, Buchenau U, Richter D, Masciovecchio C, Sette F, Mermet A, Fioretto D, Ruocco G, Willner L and Frick B 1999 *Phys. Rev.* E **60** R2464
Masciovecchio C, Mermet A, Ruocco G and Sette F 2000 *Phys. Rev. Lett.* **85** 1266
Matic A, Engberg D, Masciovecchio C and Borjesson L 2001 *Phys. Rev. Lett.* **86** 3803
Matic A, Borjesson L, Ruocco G, Masciovecchio C, Mermet A, Sette F and Verbeni R 2001 *Europhys. Lett.* **54** 7783
[5] Foret M, Courtens E, Vacher R and Suck J-B 1996 *Phys. Rev. Lett.* **77** 3831
[6] Benassi P, Krisch M, Masciovecchio C, Mazzacurati V, Monaco G, Ruocco G, Sette F and Verbeni R 1996 *Phys. Rev. Lett.* **77** 3835
[7] Foret M, Courtens E, Vacher R and Suck J-B 1997 *Phys. Rev. Lett.* **78** 4670
[8] Benassi P, Krisch M, Masciovecchio C, Mazzacurati V, Monaco G, Ruocco G, Sette F and Verbeni R 1997 *Phys. Rev. Lett.* **78** 4669
[9] Masciovecchio C, Ruocco G, Sette F, Benassi P, Cunsolo A, Krisch M, Mazzacurati V, Mermet A, Monaco G and Verbeni R 1997 *Phys. Rev.* B **55** 8049
[10] Masciovecchio C, Mazzacurati V, Monaco G, Ruocco G, Scopigno T, Sette F, Benassi P, Cunsolo A, Fontana A, Krisch M, Mermet A, Montagna M, Rossi F, Sampoli M, Signorelli G and Verbeni R 1999 *Phil. Mag.* **79** 2013
[11] Rat E, Foret M, Courtens E, Vacher R and Arai M 1999 *Phys. Rev. Lett.* **83** 1355
[12] Pilla O, Cunsolo A, Fontana A, Masciovecchio C, Monaco G, Montagna M, Ruocco G, Scopigno T and Sette F 2000 *Phys. Rev. Lett.* **85** 2136
[13] Sette F, Ruocco G, Krisch M, Bergmann U, Masciovecchio C, Mazzacurati V, Signorelli G and Verbeni R 1995 *Phys. Rev. Lett.* **75** 850
Ruocco G, Sette F, Krisch M, Bergmann U, Masciovecchio C, Mazzacurati V, Signorelli G and Verbeni R 1996 *Nature* **379** 521

Sinn H, Sette F, Bergmann U, Halcoussis C, Krisch M, Verbeni R and Burkel E 1997 *Phys. Rev. Lett.* **78** 1715
Ruocco G, Sette F, Krisch M, Bergmann U, Masciovecchio C and Verbeni R 1996 *Phys. Rev.* B **54** 14 892
Monaco G, Masciovecchio C, Ruocco G and Sette F 1998 *Phys. Rev. Lett.* **80** 2161
Cunsolo A, Pratesi G, Ruocco G, Sampoli M, Sette F, Verbeni R, Barocchi F, Krisch M, Masciovecchio C and Nardone M 1998 *Phys. Rev. Lett.* **80** 3515
Cunsolo A, Ruocco G, Sette F, Masciovecchio C, Mermet A, Monaco G, Sampoli M and Verbeni R 1999 *Phys. Rev. Lett.* **82** 775
Ruocco G and Sette F 1999 *J. Phys.: Condens. Matter* **11** R259
Monaco G, Cunsolo A, Ruocco G and Sette F 1999 *Phys. Rev.* E **60** 5505
Scopigno T, Balucani U, Cunsolo A, Masciovecchio C, Ruocco G, Sette F and Verbeni R 2000 *Europhys. Lett.* **50** 189
Sette F, Ruocco G, Cunsolo A, Masciovecchio C, Monaco G and Verbeni R 2000 *Phys. Rev. Lett.* **84** 4136
Scopigno T, Balucani U, Ruocco G and Sette F 2000 *Phys. Rev. Lett.* **85** 4076
Hosokawa S, Kawakita Y, Pilgrim W C and Sinn H 2001 *Phys. Rev.* B **63** 134205
Scopigno T, Balucani U, Ruocco G and Sette F 2001 *Phys. Rev.* E **63** 011210
Cunsolo A, Pratesi G, Verbeni R, Colognesi D, Monaco G, Masciovecchio C, Ruocco G and Sette F 2001 *J. Chem. Phys.* at press
Scopigno T, D'Astuto M, Krisch M, Sette F and Ruocco G 2001 *Phys. Rev.* B **64** 012301
Chen S H, Liao C Y, Huang H W, Weiss T M, Bellisent-Funel M C and Sette F 2001 *Phys. Rev. Lett.* **86** 740
Verbeni R, Cunsolo A, Pratesi G, Monaco G, Rosica F, Masciovecchio C, Nardone M, Ruocco G, Sette F and Albergamo F 2001 *Phys. Rev.* E at press

[14] Sette F, Ruocco G, Krisch M, Masciovecchio C, Verbeni R and Bergmann U 1996 *Phys. Rev. Lett.* **77** 83

[15] Ruocco G, Sette F, Di Leonardo R, Fioretto D, Lorentzen M, Krisch M, Masciovecchio C, Monaco G, Pignon F and Scopigno T 1999 *Phys. Rev. Lett.* **83** 5583

[16] Mazzacurati V, Ruocco G and Sampoli M 1996 *Europhys. Lett.* **34** 681
Taraskin S N and Elliott S R 1997 *Europhys. Lett.* **39** 37
Taraskin S N and Elliott S R 1997 *Phys. Rev.* B **56** 8605
Ribeiro M C C, Wilson M and Madden P A 1998 *J. Chem. Phys.* **108** 9027
Ribeiro M C C, Wilson M and Madden P A 1998 *J. Chem. Phys.* **109** 9859
Sampoli M, Benassi P, Dell'Anna R, Mazzacurati V and Ruocco G 1998 *Phil. Mag.* **77** 473
Fabian J and Allen P B 1999 *Phys. Rev. Lett.* **82** 1478
Feldman J L, Allen P B and Bickham S R 1999 *Phys. Rev.* B **59** 3551
Taraskin S N and Elliott S R 2000 *Phys. Rev.* B **61** 12 017
Taraskin S N and Elliott S R 2000 *Phys. Rev.* B **61** 12 031
Mossa S, Monaco G, Ruocco G, Sampoli M and Sette F 2001 *Preprint* cond-mat/0104129

[17] Dell'Anna R 1997 *PhD Thesis* University of L'Aquila, I

[18] Dell'Anna R, Ruocco G, Sampoli M and Viliani G 1998 *Phys. Rev. Lett.* **80** 1236

[19] Horbach J, Kob W and Binder K 2001 *Eur. Phys. J.* B **19** 531

[20] Benoit C, Royer E and Poussigue G 1992 *J. Phys.: Condens. Matter* **4** 3125

[21] Schirmacher W, Diezemann G and Ganter C 1998 *Phys. Rev. Lett.* **81** 136

[22] Taraskin S N, Loh Y L, Natarajan G and Elliott S R 2001 *Phys. Rev. Lett.* **86** 1255

[23] Martin-Mayor V, Parisi G and Verrocchio P 2000 *Phys. Rev.* E **62** 2373

[24] Angelani L, Montagna M, Ruocco G and Viliani G 2000 *Phys. Rev. Lett.* **84** 4874

[25] Ruocco G, Sette F, Di Leonardo R, Monaco G, Sampoli M, Scopigno T and Viliani G 2000 *Phys. Rev. Lett.* **84** 5788

[26] Duval E and Mermet A 1998 *Phys. Rev.* B **58** 8159

[27] Verbeni R, Sette F, Krisch M, Bergmann U, Gorges B, Halcoussis C, Martel K, Masciovecchio C, Ruocco G and Sinn H 1996 *J. Synchrotron Radiat.* **3** 62
Masciovecchio C, Bergmann U, Krisch M, Ruocco G, Sette F and Verbeni R 1996 *Nucl. Instrum. Methods* B **111** 181
Masciovecchio C, Bergmann U, Krisch M, Ruocco G, Sette F and Verbeni R 1996 *Nucl. Instrum. Methods* B **117** 339

[28] Vashista P, Kalia R K and Rino J P 1990 *Phys. Rev.* B **41** 12 197

[29] Stillinger F H and Weber T A 1983 *Phys. Rev.* A **28** 2408

[30] Viliani G, Dell'Anna R, Pilla O, Ruocco G, Signorelli G and Mazzacurati V 1995 *Phys. Rev.* B **52** 3346

[31] Balucani U and Zoppi M 1994 *Dynamics of the Liquid State* (Oxford: Clarendon)

[32] Scopigno T, Balucani U, Ruocco G and Sette F 2000 *J. Phys.: Condens. Matter* **12** 8009

[33] Zhu T C, Maris H J and Tauc J 1991 *Phys. Rev.* B **44** 4281

Zhu T C, Maris H J and Tauc J 1990 *Phonon 89* ed S Hunklinger, W Ludwig and G Weiss (Singapore: World Scientific) pp 498, 1430
[34] Pine A 1969 *Phys. Rev.* **185** 1187
Bucaro J A and Dardy H D 1974 *J. Appl. Phys.* **45** 5324
Vacher R and Pelous J 1976 *Phys. Rev.* B **14** 823
Vacher R, Sussner H and Hunklinger S 1980 *Phys. Rev.* B **21** 5850
[35] Wischnewski A, Buchenau U, Dianoux A J, Kamitakahara W A and Zaretsky C 1998 *Phys. Rev.* B **57** 2663
[36] Theenhaus T, R Schilling, Latz A and Letz M 2001 *Preprint* cond-mat/0105393
[37] Sampoli M, Ruocco G and Sette F 1997 *Phys. Rev. Lett.* **79** 1678
[38] Pilla O *et al* 2001 *Preprint*